A Power-Enhancing Complementary Coupling Integration Strategy for Misalignment-Tolerant WPT Systems

Zhaoyang Yuan, *Member, IEEE*, Qingxin Yang, Xian Zhang, Ran Wang, Xianjie Ma, Changsong Cai, *Senior Member, IEEE*, Pengcheng Zhang, *Senior Member, IEEE*, Hongjian Lin, *Senior Member, IEEE*, and Maryam Saeedifard, *Fellow, IEEE*

***Abstract*—This article presents a complementary coupling integration method for an inductor–capacitor–capacitor-series-compensated wireless power transfer (WPT) system to improve the misalignment tolerance and power transfer capability. To this end, a compensation (Cx) coil formed by a long rectangular coil wound into a C-shaped structure is proposed. As a result, two multiples of the mutual inductance (MI) between the Cx and receiver (Rx) coils are added to the MI between the transmitter and Rx coils, providing the MI complement effect to increase the equivalent MI under both the perfectly aligned and misaligned conditions. A mathematical model based on the Delta–Wye network transform is developed to obtain the zero-phase-angle (ZPA) input and load-independent constant current (CC) output conditions. A 1-kW scaled-down WPT prototype based on the proposed method is built, and its performance is experimentally validated. The proposed system achieves 85.22% efficiency at 150-mm air gap and tolerates ±200-mm x-, y-, and diagonal misalignments, ±50-mm z-misalignment, and 20° angular misalignment with ZPA input and load-independent CC output as the load varies from 5 to 20 Ω. In addition, the system performance is barely affected by the planar rotation misalignment.**

***Index Terms*—Complementary coupling integration, constant current (CC) output, misalignment tolerance, power enhancement, wireless power transfer (WPT).**

Manuscript received 24 May 2023; revised 10 July 2023; accepted 1 August 2023. Date of publication 7 August 2023; date of current version 22 September 2023. This work was supported in part by the National Natural Science Foundation of China under Grants 52122701, 51977147, and 52207010 and in part by the National Science Foundation of Tianjin City, China, under Grant 22JCZDJC00620. Recommended for publication by Associate Editor Alon Kuperman. *(Corresponding author: Qingxin Yang.)*

Zhaoyang Yuan, Xian Zhang, Ran Wang, and Xianjie Ma are with the State Key Laboratory of Reliability and Intelligence of Electrical Equipment, Hebei University of Technology, Tianjin 300401, China (e-mail: zyyuan@ieee.org; zhangxian@hebut.edu.cn; rwangeeri@163.com; maxhebut@163.com).

Qingxin Yang is with the Tianjin University of Technology, Tianjin 300384, China (e-mail: qxyang@tjut.edu.cn).

Changsong Cai is with the School of Electrical Engineering and Automation, Wuhan University, Wuhan 430072, China (e-mail: changsongcai@whu.edu.cn).

Pengcheng Zhang is with the Department of Electrical Engineering, Tsinghua University, Beijing 100084, China (e-mail: pczhang@mail.tsinghua.edu.cn).

Hongjian Lin is with the Department of Electrical Engineering, City University of Hong Kong, Hong Kong (e-mail: hongjlin@um.cityu.edu.hk).

Maryam Saeedifard is with the School of Electrical and Computer Engineering, Georgia Institute of Technology, Atlanta, GA 30332 USA (e-mail: maryam@ece.gatech.edu).

Color versions of one or more figures in this article are available at https://doi.org/10.1109/TPEL.2023.3302699.

Digital Object Identifier 10.1109/TPEL.2023.3302699

I. Introduction

WIRELESS power transfer (WPT) is gaining traction as a promising way for charging electric vehicles (EVs) [1], [2]. In the WPT systems, the primary transmitter (Tx) and secondary receiver (Rx) coils are tuned to magnetic resonance at the operating frequency and meet the highly resonant conditions to enhance the power transfer. The coupling coefficient k between the Tx and Rx coils is a critical design parameter to enhance power transfer capability and efficiency [2]. However, from practical perspectives, the constant output and maximum efficiency cannot be guaranteed due to the load variation and reduction of k affected by the misalignment between the Tx and Rx coils. Therefore, the design of load-independent output, i.e., constant current (CC) and/or constant voltage (CV) outputs, is necessary to enhance a wide load variation range [1]. As k has a positive correlation with the mutual inductance (MI), the misalignment tolerance of the MI is the focus of the WPT system design.

Several control schemes have been proposed to achieve the desired CC and/or CV outputs, as well as improve misalignment tolerance. These schemes include the utilization of additional dc–dc converters, frequency tuning, phase-shift control, duty-cycle control, load identification, and hybrid control strategies [2], [3]. In addition, achieving wider load adaptability necessitates high-performance control and the use of larger components. To address this, self-tuning methods based on switched components with simplified control parameters have been proposed. These methods aim to enhance misalignment tolerance and optimize system performance [4], [5]. Furthermore, in [6], a controlled capacitor matrix is designed, while Zhang et al. [7] introduce a continuously controlled variable inductor. However, in order to provide a substantial tolerance to misalignment and load variation, it is crucial to design the controlled composition components with a wide resonant matching range [8]. On top of the potential additional costs, there might be reliability concerns associated with the speed and accuracy of the control mechanism.

The design of the compensation (Cx) topologies, such as series–series (SS) [9], series–series–parallel [10], series-capacitor–inductor–capacitor [11], inductor–capacitor–capacitor-series (LCC-S) [12], and LCC–LCC [13], is another

approach to tolerate the MI and load variations. A detuned design method based on the sensitivity of k is proposed for a family of Cx topologies [10], [14]. However, this design approach is complex, and the reactive power due to the nonresonant state increases the cost. In [15], an X-type $LLCC$ Cx topology is proposed, which has a stable power transfer capacity without requiring any dedicated coil design or precise control. Another approach is presented in [16], where a reconfigurable topology based on the equivalent detuned SS topology is proposed. Under different load conditions, the two equivalent detuned SS topologies can be switched at the crossover coupling coefficient point by employing an ac switch to obtain the constant transfer power–coupling coefficient curves. To address the limitation of SS topology under large misalignments, a switchable topology that transitions between the SS and $LCCC$-S configurations is proposed in [17]. However, improving misalignment tolerance capability solely based on the Cx topology design is insufficient.

Further improvement in misalignment tolerance can be achieved by incorporating special magnetic couplers in conjunction with the Cx topology design [18], [19], [20], [21]. Moreover, the integration of coils is employed to reduce the number of components, power loss, and volume. The reversed-series structure coils are also proposed as a means to improve the misalignment tolerance capability [22]. However, when designing a constant MI difference between the primary and secondary coils, it leads to a decrease in the equivalent MI, thereby reducing power transfer capacity. To address this issue, Zhang et al. [23] propose the design of the Cx and Tx coils of the LCL-S topology as identical reversed-series structures, firmly attached to enhance the flux density. While this approach reduces reactive power loss, it also imposes restrictions on the available topology options. Furthermore, Yuan et al. [24] introduce a misalignment-tolerant design based on a cost function optimization to increase the degree of freedom in coil design and eliminate restrictions on the correlation of MI variations between the primary and secondary coils. Nevertheless, the inherent reduction in the equivalent MI of reversed-series structure coils can result in a substantial increase in the output power and a surge in the input current when it exceeds the tolerance range, potentially leading to system failure. This challenge remains to be fully resolved in [23] and [24].

In order to maintain the equivalent MI and enhance misalignment tolerance capability on the horizontal plane, several coil configurations have been proposed. These include multiple double-D (DD) coils [25], double solenoid quadrature coupler coils [26], compact double-D quadrature pad coils [27], [28], and compact quadruple-D quadrature pad coils [29]. These coil configurations are combined with hybrid Cx topology designs to achieve the desired performance.

By considering the opposite gain trends of the two hybrid Cx topologies under misalignment conditions, the equivalent MI can be stabilized [28]. Qu et al. [30] propose a general design method for a family of hybrid Cx topologies. However, these designs are primarily focused on compensating for the equivalent MI under misaligned conditions to match the value in the perfectly aligned state and do not have the capability to enhance the equivalent MI in order to improve power transfer capacity. In addition, under the perfectly aligned condition, the MI-complemented coil is decoupled from the Rx coil and remains uninvolved in the power transfer process, leading to power loss.

An integrated LCC-S-compensated dual-Tx dual-Rx system is proposed in [31], which improves the equivalent MI under the perfectly aligned condition, albeit to a minimal extent. This system achieves the decoupling of the two coils in the main coil, and the low-power area is eliminated by connecting two unipolar coils in series. However, this approach does not integrate the space-occupant and high-power-loss Cx inductors. Moreover, simultaneous achievement of misalignment tolerance for both the Rxs under the x-misalignment condition is not feasible in this system.

To improve the misalignment tolerance and power transfer capacity, particularly in scenarios involving light EVs, automated guided vehicles (AGVs), and similar applications, this article introduces an integrated magnetic coupler topology combined with a misalignment tolerant strategy based on the LCC-S-compensated WPT system. The main contributions of this article are summarized as follows.

1) A novel integrated magnetic coupler topology that incorporates a complementary coupling effect is introduced. Under misalignment conditions, the gain trends of the Cx and Tx coils exhibit opposite behavior compared to the MI. This unique characteristic is leveraged in the design to enhance performance. In contrast to previous designs employing hybrid Cx topologies, the proposed design eliminates the need for coil decoupling considerations. Instead, it focuses on enhancing the equivalent MI and power transfer capacity by adding multiples of the MI between the Cx and Rx coils to the MI between the Tx and Rx coils.
2) The misalignment tolerance and output characteristics of the integrated LCC-S topology are analyzed. Then, a power-improving design method for the Cx topology is proposed, achieving the load-independent CC output with misalignment tolerance.

The rest of this article is organized as follows. Section II focuses on analyzing the requirements of the zero-phase-angle (ZPA) input and load-independent CC output for the integrated LCC-S topology. Section III introduces the proposed integrated coil structure and outlines the design methodology for achieving misalignment tolerance. Experimental results for the proposed design are provided in Section IV. Finally, Section V concludes this article.

II. System Configuration and Design

A. Equivalent Circuit Derivation and Cx Design

The circuit of the proposed LCC-S-compensated WPT system is shown in Fig. 1, where V_{dc} is the dc input voltage and $\boldsymbol{V}_{\mathrm{in}}$ is the H-bridge inverter output voltage with the nominal operating frequency of 85 kHz on the primary side. L_{f}, L_{p}, and L_{s} are the inductances of the Cx, Tx, and Rx coils, respectively. As presented in Fig. 1 with red dashed arrows, the MIs between the Cx and Tx coils, the Cx and Rx coils, and the Tx and Rx

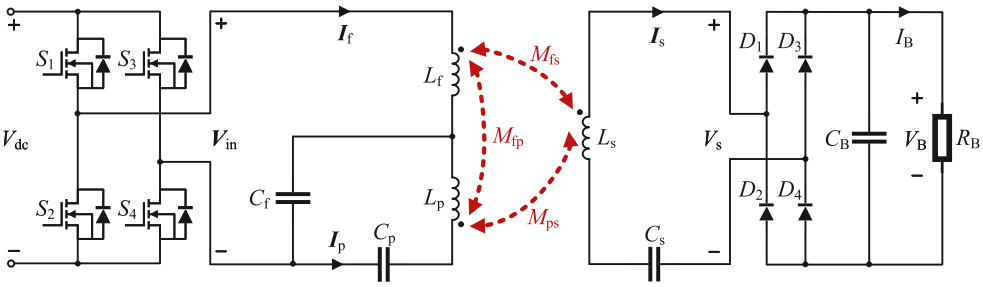

Fig. 1. Circuit configuration of the WPT system based on the LCC-S-compensated topology.

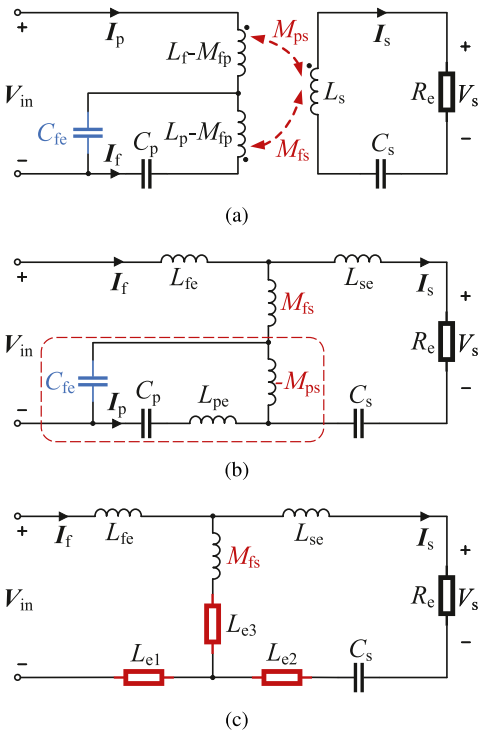

Fig. 2. Equivalent circuit of the proposed LCC-S-compensated WPT system. (a) M_{fp} is decoupled. (b) T-model. (c) Simplified circuit by the Delta–Wye network transform.

coils are defined as M_{fp}, M_{fs}, and M_{ps}, respectively. C_f, C_P, and C_s are the resonant capacitors to the Cx, Tx, and Rx coils, respectively. $\boldsymbol{I}_f$, $\boldsymbol{I}_p$, and $\boldsymbol{I}_s$ are the currents flowing through the Cx, Tx, and Rx coils, respectively. $\boldsymbol{V}_s$ is the input voltage of the diode bridge rectifier on the secondary side. C_B is the filtering capacitor. I_B and V_B are the dc charging current and voltage, respectively. R_B is an equivalent resistance to model the battery, where $R_B = V_B/I_B$.

The equivalent circuit of Fig. 1 can be simplified to the circuit shown in Fig. 2(a), in which

$$C_{fe} = \frac{C_f}{1-\omega^2 M_{fp} C_f} \tag{1a}$$

$$V_{in} = \frac{2\sqrt{2}}{\pi} V_{dc} \tag{1b}$$

$$R_e = \frac{8R_B}{\pi^2} \tag{1c}$$

where R_e is the equivalent resistance observed before the rectifier. Based on the loosely coupled transformer, the primary and secondary coils can be modeled by the T-model, as shown in Fig. 2(b). Based on the Delta–Wye network transform and defining

$$L_{fe} = L_f - M_{fs} - M_{fp} \tag{2a}$$

$$L_{pe} = L_p + M_{ps} - M_{fp} \tag{2b}$$

$$L_{se} = L_s + M_{ps} - M_{fs} \tag{2c}$$

the circuit in Fig. 2(b) can be further simplified as the circuit shown in Fig. 2(c), where

$$L_{e1} = -\frac{\omega^2 L_{pe} C_p - 1}{\omega^2 \left(\left(\omega^2 \left(L_{pe} - M_{ps}\right) C_{fe} - 1\right) C_p - C_{fe}\right)} \tag{3a}$$

$$L_{e2} = -\frac{\left(\omega^2 L_{pe} C_p - 1\right) M_{ps} C_{fe}}{\left(\omega^2 \left(L_{pe} - M_{ps}\right) C_{fe} - 1\right) C_p - C_{fe}} \tag{3b}$$

$$L_{e3} = \frac{M_{ps} C_p}{\left(\omega^2 \left(L_{pe} - M_{ps}\right) C_{fe} - 1\right) C_p - C_{fe}}. \tag{3c}$$

The equivalent circuit is shown in Fig. 2(c) and can be modeled by

$$Z_{fe} \boldsymbol{I}_f - j\omega \left(L_{e3} + M_{fs}\right) \boldsymbol{I}_s = \boldsymbol{V}_{in} \tag{4a}$$

$$-j\omega \left(L_{e3} + M_{fs}\right) \boldsymbol{I}_f + Z_{se} \boldsymbol{I}_s = -R_e \boldsymbol{I}_s \tag{4b}$$

in which

$$Z_{fe} = j\omega \left(L_{fe} + L_{e1} + L_{e3} + M_{fs}\right) \tag{5a}$$

$$Z_{se} = j\omega \left(L_{se} + L_{e2} + L_{e3} + M_{fs}\right) + \frac{1}{j\omega C_s}. \tag{5b}$$

Based on (4), the input impedance Z_{in} of the equivalent circuit shown in Fig. 2(c) is given as

$$Z_{in} = Z_{fe} + \frac{\omega^2 \left(L_{e3} + M_{fs}\right)^2}{Z_{se} + R_e}. \tag{6}$$

In (6), when

$$Z_{fe} = 0, \quad Z_{se} = 0 \tag{7}$$

the imaginary part of Z_{in} equals zero, and a purely resistive input impedance is achieved and expressed as

$$Z_{\text{in}} = \frac{\omega^2 \left(L_{\text{e3}} + M_{\text{fs}}\right)^2}{R_{\text{e}}}. \tag{8}$$

By substituting (1)–(3) and (5) into (7), the Cx capacitors can be derived as

$$C_{\text{p}} = \frac{\alpha}{\omega^2 \left(\alpha \left(L_{\text{p}} - M_{\text{fp}}\right) - \left(L_{\text{f}} - M_{\text{fp}}\right)\right)} \tag{9a}$$

$$C_{\text{s}} = \frac{L_{\text{f}} - M_{\text{fp}}}{\omega^2 \left(L_{\text{s}} \left(L_{\text{f}} - M_{\text{fp}}\right) - \alpha \left(\alpha + 1\right) M_{\text{ps}}^2\right)} \tag{9b}$$

in which

$$\alpha = \omega^2 \left(L_{\text{f}} - M_{\text{fp}}\right) C_{\text{fe}} - 1. \tag{10}$$

It should be emphasized that the relation of C_{s} in (9b) cannot be maintained due to the change of M_{ps} caused by the misalignment. Therefore, the ZPA-based resonance of the circuit will be lost. To mitigate the impacts of the misalignment on the system performance, (9b) is modified to

$$C_{\text{s}} = \frac{1}{\omega^2 L_{\text{s}}}. \tag{11}$$

Therefore, the currents in coils can be derived based on (9) and (11) as

$$\boldsymbol{I}_{\text{f}} = \frac{R_{\text{e}} \boldsymbol{V}_{\text{in}}}{\omega^2 \left(M_{\text{fs}} - \alpha M_{\text{ps}}\right)^2} - j \frac{\alpha \omega M_{\text{ps}}^2 C_{\text{fe}} \boldsymbol{V}_{\text{in}}}{\left(M_{\text{fs}} - \alpha M_{\text{ps}}\right)^2} \tag{12a}$$

$$\boldsymbol{I}_{\text{p}} = -\frac{\alpha R_{\text{e}} \boldsymbol{V}_{\text{in}}}{\omega^2 \left(M_{\text{fs}} - \alpha M_{\text{ps}}\right)^2} + j \frac{\alpha \omega M_{\text{fs}} M_{\text{ps}} C_{\text{fe}} \boldsymbol{V}_{\text{in}}}{\left(M_{\text{fs}} - \alpha M_{\text{ps}}\right)^2} \tag{12b}$$

$$\boldsymbol{I}_{\text{s}} = j \frac{\boldsymbol{V}_{\text{in}}}{\omega \left(M_{\text{fs}} - \alpha M_{\text{ps}}\right)}. \tag{12c}$$

As can be found from (12c), based on the compensated condition in (9a) and (11), the circuit shown in Fig. 1 can offer a load-independent CC output.

B. System Efficiency and Power Improvement

The input active and reactive powers can be obtained by

$$P_{\text{in}} = \Re\left\{\boldsymbol{V}_{\text{in}} \boldsymbol{I}_{\text{f}}^*\right\} = \frac{R_{\text{e}} \boldsymbol{V}_{\text{in}}^2}{\omega^2 \left(M_{\text{fs}} - \alpha M_{\text{ps}}\right)^2} \tag{13}$$

$$Q_{\text{in}} = \Im\left\{\boldsymbol{V}_{\text{in}} \boldsymbol{I}_{\text{f}}^*\right\} = \frac{\alpha \omega M_{\text{ps}}^2 C_{\text{fe}} \boldsymbol{V}_{\text{in}}^2}{\left(M_{\text{fs}} - \alpha M_{\text{ps}}\right)^2}. \tag{14}$$

To obtain the maximum system efficiency, the reactive power Q_{in} should be significant small. Therefore, to obtain the ideally compensated condition ensuring maximum system efficiency, C_{fe} should be optimally determined. Based on (13) and (14), let the ratio of Q_{in} over P_{in} be

$$\tau = \frac{Q_{\text{in}}}{P_{\text{in}}} = \frac{\alpha \omega^3 M_{\text{ps}}^2 C_{\text{fe}}}{R_{\text{e}}}. \tag{15}$$

Solving the derivative of τ with respect to C_{fe}, the ideally compensated condition to obtain the maximum system efficiency of the Cx topology is derived as

$$\begin{cases} \dfrac{d\tau}{dC_{\text{fe}}} = 0 \\ \dfrac{d^2\tau}{dC_{\text{fe}}^2} > 0 \end{cases}, \quad \Rightarrow \quad C_{\text{fe}} = \frac{1}{2\omega^2 \left(L_{\text{f}} - M_{\text{fp}}\right)}. \tag{16}$$

Based on (16), (15) can be rewritten as

$$\tau = -\frac{\omega M_{\text{ps}}^2}{4 \left(L_{\text{f}} - M_{\text{fp}}\right) R_{\text{e}}} \ll 1. \tag{17}$$

Consequently, (12) can be simplified as

$$\boldsymbol{I}_{\text{f}} \approx \frac{4 R_{\text{e}} \boldsymbol{V}_{\text{in}}}{\omega^2 \left(M_{\text{ps}} + 2M_{\text{fs}}\right)^2} \tag{18a}$$

$$\boldsymbol{I}_{\text{p}} \approx \frac{2 R_{\text{e}} \boldsymbol{V}_{\text{in}}}{\omega^2 \left(M_{\text{ps}} + 2M_{\text{fs}}\right)^2} \tag{18b}$$

$$\boldsymbol{I}_{\text{s}} = j \frac{2 \boldsymbol{V}_{\text{in}}}{\omega \left(M_{\text{ps}} + 2M_{\text{fs}}\right)} \tag{18c}$$

where the Cx conditions are simplified as

$$C_{\text{p}} = \frac{1}{\omega^2 \left(L_{\text{p}} + 2L_{\text{f}} - 3M_{\text{fp}}\right)} \tag{19a}$$

$$C_{\text{f}} = \frac{1}{\omega^2 \left(2L_{\text{f}} - M_{\text{fp}}\right)}. \tag{19b}$$

As can be found from (18), under the maximum-efficiency-based Cx conditions, the system can offer the near-ZPA input.

The output active power P_{o} can be derived as

$$P_{\text{o}} = \left|\boldsymbol{I}_{\text{s}}^2 R_{\text{e}}\right| = \frac{4 \boldsymbol{V}_{\text{in}}^2 R_{\text{e}}}{\omega^2 \left(M_{\text{ps}} + 2M_{\text{fs}}\right)^2} = \frac{4 \boldsymbol{V}_{\text{in}}^2 R_{\text{e}}}{\omega^2 M_{\text{eq}}^2} \tag{20}$$

where $M_{\text{eq}} = M_{\text{ps}} + 2M_{\text{fs}}$ is the equivalent MI of the proposed design.

In comparison to the literature involving CC output, such as the SS [32], LCL-S [23], and LCC–LCC [18] topologies, and assuming an identical system configuration, the power ratios can be derived as

$$\lambda_1 = \frac{P_{\text{o}}}{P_{\text{o}-\text{SS}}} = \frac{4M_{\text{ps}}^2}{M_{\text{eq}}^2} > 1 \tag{21a}$$

$$\lambda_2 = \frac{P_{\text{o}}}{P_{\text{o}-LCL}} = \frac{16M_{\text{ps}}^2}{M_{\text{eq}}^2} > 4 \tag{21b}$$

$$\lambda_3 = \frac{P_{\text{o}}}{P_{\text{o}-LCC}} = \frac{4L_{\text{f1}}^2 L_{\text{f2}}^2}{M_{\text{ps}}^2 M_{\text{eq}}^2} < \frac{L_{\text{f1}}^2 L_{\text{f2}}^2}{M_{\text{ps}}^4} \tag{21c}$$

where the subscripts "$-$SS," "$-LCL$," and "$-LCC$" refer to the system with SS, LCL-S, and LCC–LCC topologies, respectively.

Owing to the opposite gain trend of M_{ps} and M_{fs} under misalignment conditions, in order to obtain a constant equivalent MI, based on the complementary coupling effect, M_{fs} is smaller than M_{ps} and, consequently, $M_{\text{eq}} < 2M_{\text{ps}}$. Therefore, λ_1 is larger than 1 and λ_2 is larger than 4, indicating an increase in the delivered power of the proposed design. Since L_{f1} and L_{f2} can be adjusted, the proposed design has the ability to offer an output power comparable to that of the LCC–LCC topology.

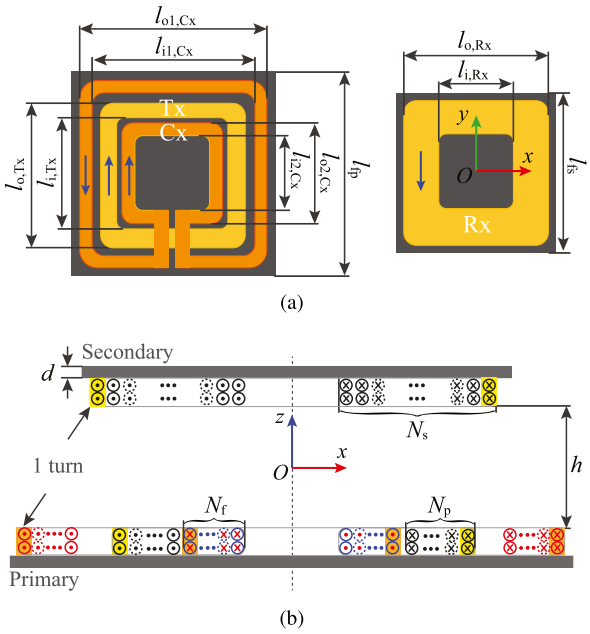

Fig. 3. (a) Coil structures on the primary and secondary sides. (b) Cross-sectional view.

III. Coil Structure and Misalignment Tolerance Design

Since the Cx and Tx coils are integrated into the primary side, M_{fp} is constant. Based on (12), to achieve a stable output within the misalignment range, the requirement can be presented as

$$M_{eq} = M_{ps} + 2M_{ps} = \text{Constant}. \tag{22}$$

Based on the abovementioned analysis, to achieve at least 50% of the length of the Rx coil misalignment tolerant range, the design objectives of the coils can be summarized as follows.

1) The trend of M_{fs} and M_{ps} versus the misalignment should be the opposite to achieve a stable M_{eq}.
2) To obtain a larger misalignment tolerant range, M_{fs} should increase at least within 50% of the length of the Rx coil misalignment range.
3) The change in the equivalent MI M_{eq} due to misalignment should be minimized to maintain the CC output profile.

Let the mean value of a set of equivalent MIs be

$$\overline{M}_{eq} = \frac{\sum M_{eq}}{N} \tag{23}$$

where $N = \frac{180}{D} + 1$ is the set size (D is the step size of misalignment) and the maximum change of M_{eq} is calculated by

$$\delta = \max\left\{\frac{M_{eq-max} - \overline{M}_{eq}}{\overline{M}_{eq}}, \frac{M_{eq-min} - \overline{M}_{eq}}{\overline{M}_{eq}}\right\} \times 100\% < 10\% \tag{24}$$

where M_{eq-max} and M_{eq-min} are the maximum and minimum values of M_{eq} in the set, respectively.

To meet the objectives, the proposed coil structures are presented in Fig. 3. The Tx and Rx coils are square shaped, while the Cx coil takes the form of a C-shaped coil, which is formed by winding a long rectangular coil around the Tx coil. The Cx coil is optimized by changing the number of turns and dimensions to achieve the misalignment tolerance. The blue arrows in Fig. 3 show the direction of the currents flowing through the coils.

The coils are wound in a two-layer parallel configuration using Litz wire $\phi = 3$ mm in diameter, as shown in Fig. 3. Considering the applications context for light EVs and AGVs, the Tx and Rx coils have the same outer length of $l_{o,Tx} = l_{o,Rx} = 360$ mm. The wire spacing of the Tx and Rx coils is 3 mm, and the numbers of turns of the Tx and Rx coils are $N_p = 5$ and $N_s = 18$, respectively. By setting the initial value of $l_{i1,Cx}$ at 360 mm, the outer length of the outer part of Cx coil is $l_{o1,Cx} = l_{i1,Cx} + 2\phi N_f$ mm. For at least 50% of the length of the Rx coil misalignment tolerant design, as shown in Fig. 3(a), the inactive area of the primary coil for the misalignment tolerance needs to be increased by designing a larger Cx coil, which, however, results in more magnetic flux leakage. Therefore, to ensure sufficient M_{fs} within a limited coil size providing a complementary coupling effect, the Cx coil is closely wound and composed of N_f turns. N_f is limited to 10 and increases from an initial value of 4 in steps of 2. The value of $l_{i1,Cx}$ is increased and limited to 420 mm by a step size of 20 mm. The initial outer length of the inner part of the Cx coil is set to be 300 mm, which decreases with the misalignment in steps of 20 mm. The inner length of the Cx coil is calculated as $l_{i2,Cx} = l_{o2,Cx} - 2\phi N_f$ mm. The outer lengths of the ferrite shielding, which has an initial permeability of 3300 on the primary and secondary sides, are $l_{fp} = l_{o1,Cx} + 20$ mm and $l_{fs} = 380$ mm, respectively. The thickness of the ferrite is $d = 2.5$ mm. The primary and secondary coils within the misalignment range are placed in two perfect parallel planes with $h = 150$-mm air gap. The number of turns of Cx coil N_f is optimally designed to meet the requirements. Since the coil structures are symmetrical, the system yields the same output under the x- and y-misalignments. Based on x-misalignment, the design flowchart of the Cx coil is shown in Fig. 4.

To improve the optimization efficiency for M_{eq}, the value and polarity of M_{fs} are compared.

1) To achieve at least 50% of the length of the Rx coil misalignment tolerant range, M_{fs} should increase as the misalignment increases from 0 to 180 mm. Therefore, M_{fs} reaches its maximum of at least 180-mm misalignment. In other words, there should be $|M_{fs-180}| > |M_{fs-160}|$, where "−160" and "−180" mean that the misalignments are 160 and 180 mm, respectively. The number of problems to be solved can be reduced by calculating and comparing $|M_{fs-180}|$ and $|M_{fs-160}|$ first.
2) To obtain the complementary coupling effect, the polarity of M_{fs} must remain unchanged as misalignment increases. As a result, M_{eq} can be significantly enhanced under both the perfectly aligned and misaligned conditions, improving the system efficiency.

After executing the flowchart in Fig. 4, the values of N_f that achieve opposite trends in the MIs between the Tx and Rx coils and the Cx and Rx coils, for at least 50% of the length of the Rx coil misalignment tolerant range, are obtained as listed in Table I.

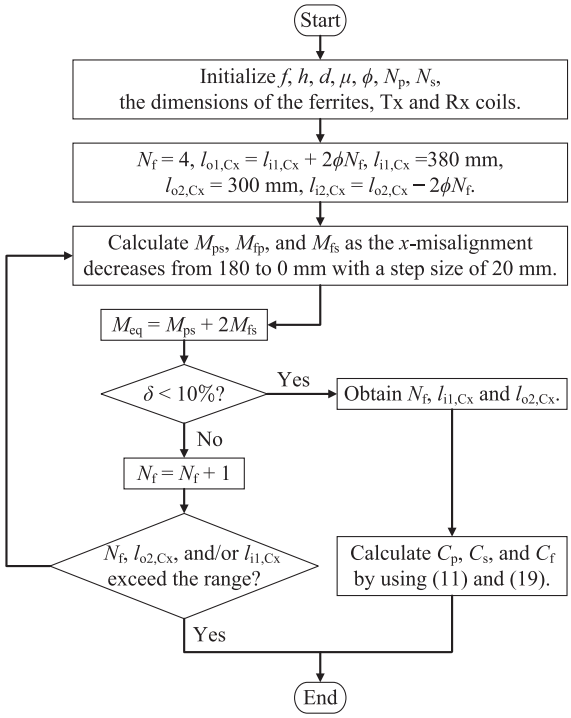

Fig. 4. Design flowchart of the Tx coil.

TABLE I
OPTIMIZATION RESULTS OF THE CX COIL

Item	N_f	$l_{i1,Cx}$	$l_{o2,Cx}$	M_{eq}	δ	Δ_{180}	Δ_{200}
#1	10	400 mm	300 mm	23.13 μH	5.87%	5.79%	10.33%
#2	8	420 mm	280 mm	23.95 μH	9.82%	7.48%	12.43%
#3	8	420 mm	300 mm	23.00 μH	9.31%	8.39%	8.39%
#4	10	420 mm	300 mm	20.10 μH	5.99%	5.77%	10.25%

For cases #1–#4, the system is capable of providing a misalignment tolerant range of 180 mm in the x-direction, while maintaining an acceptable variation in the equivalent MI. For cases #2 and #3, stable M_{eq} can be maintained with a change of 9.91% and 9.47%, which is much larger than 5.87% in case #1 and 5.99% in case #4. However, M_{eq} reaches its maximum of 23.95 μH in case #2. To determine the optimal selection, the variation Δ of the output current within the misalignment tolerant range is compared

$$\Delta = \frac{\boldsymbol{I}_{s-max} - \boldsymbol{I}_{s-min}}{\boldsymbol{I}_{s-max} + \boldsymbol{I}_{s-min}} \times 100\% = \frac{M_{eq-max} - M_{eq-min}}{M_{eq-max} + M_{eq-min}} \times 100\% < 10\%. \quad (25)$$

From Table I, it can be observed that cases #1 and #4 can provide relatively smaller output current fluctuations Δ_{180} compared with cases #2 and #3 within 180-mm misalignment range. Specifically, for case #4, $\boldsymbol{I}_s$ demonstrates the minimum fluctuation of 5.77% as x-misalignment varies from 0 to 180 mm. Nevertheless, case #4 results in a higher M_{eq} change of 5.99%, as compared to 5.87% observed in case #1. Moreover, the system outputs a higher M_{eq} of 23.13 μH in case #1 than 20.10 μH in case #4, reducing the primary volt-ampere rating to deliver the required power. Considering the objective of achieving the same misalignment tolerance capacity, case #1 outperforms case #4. When the misalignment increases to 200 mm, the smallest Δ_{200} is attained in case #3. Although case #1 performs a larger fluctuation in the output current of 10.33% compared with case #3, the resulting variance is negligible at 2.07 μH compared to the perfectly aligned condition and falls within an acceptable range. Meanwhile, a larger magnetic flux leakage occurs in cases #2–#4 due to the larger size of the Tx coil. Therefore, case #1 is selected as the optimal outcome for the Cx coil design.

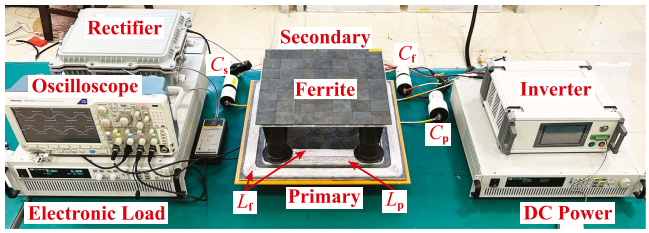

Fig. 5. Experimental setup.

TABLE II
PARAMETERS OF THE LCC-S-COMPENSATED WPT SYSTEM

Parameter	Description	Value
V_{dc}	DC power supply	84 V
P_o	Rated power	1 kW
f	Resonant frequency	84.8 kHz
d	Air gap between the pads	150 mm
R_B	Load resistance	10 Ω
σ	Initial permeability of ferrite	3300
L_f	Inductance of the Cx coil	190.01 μH
L_p	Inductance of the Tx coil	37.01 μH
L_s	Inductance of the Rx coil	179.26 μH
C_f	Cx capacitor of the Cx coil	9.49 nF
C_p	Cx capacitor of the Tx coil	8.69 nF
C_s	Cx capacitor of the Rx coil	19.74 nF
M_{fp}	MI between the Cx and Tx coils	−1.57 μH
M_{fs}	MI between the Cx and Rx coils	15.13 μH
M_{ps}	MI between the Tx and Rx coils	3.19 μH
M_{eq}	Equivalent MI	21.51 μH

IV. EXPERIMENTAL VALIDATION

A. System Setup and Operation Analysis

To demonstrate the effectiveness of the proposed design for the applications in light EVs and AGVs, a 1-kW laboratory-scaled-down experimental prototype of the optimized LCC-S-compensated WPT system is constructed and tested. The prototype is based on the optimal result obtained from case #1, as illustrated in Fig. 5. The air gap and misalignment conditions are controlled using adjustable ABS polymer feet and pads, which are magnetically transparent. The prototype parameters are listed in Table II.

When the primary and secondary coils are perfectly aligned, the steady-state waveforms of the input voltage $\boldsymbol{V}_{in}$ and current $\boldsymbol{I}_f$ and output voltage $\boldsymbol{V}_s$ and current $\boldsymbol{I}_s$ are shown in Fig. 6. These waveforms confirm the achievement of ZPA input and validate the correctness of the theoretical analysis conducted for the design.

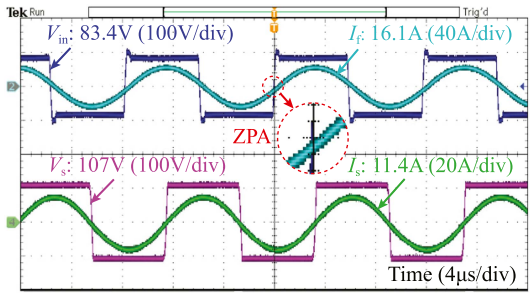

Fig. 6. Steady-state experimental waveforms of the input voltage $\boldsymbol{V}_{\mathrm{in}}$ and current $\boldsymbol{I}_{\mathrm{f}}$ and the output voltage $\boldsymbol{V}_{\mathrm{s}}$ and current $\boldsymbol{I}_{\mathrm{s}}$ under rated condition.

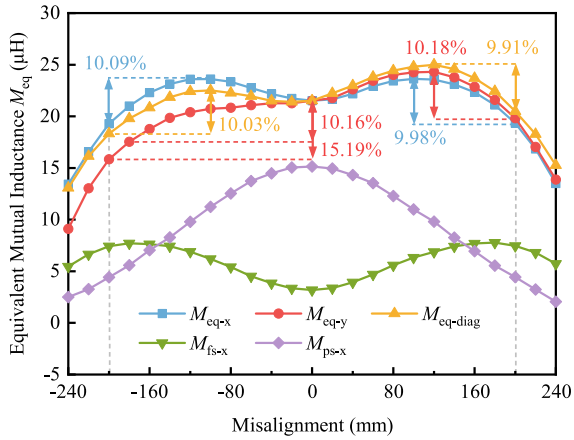

Fig. 7. Variations of M_{fs} and M_{ps} versus the x-misalignment, and the comparison of M_{eq} versus misalignment under x-, y-, and diagonal misalignments from -240 to 240 mm.

B. Horizontal Misalignment Analysis

Based on Table II, the variation of M_{eq} is calculated and analyzed under the x- and y-misalignments from -240 to 240 mm with a step size of 30 mm, as well as the diagonal misalignment that is composed of equal x- and y-misalignments, as illustrated in Fig. 7. The subscripts with "-x," "-y," and "-diag" refer to the x-, y-, and diagonal misalignments, respectively.

From Fig. 7, it can be observed that when the primary and secondary coils are perfectly aligned, M_{fs} and M_{ps} have the same polarity but the opposite gain trends of the MI under x-misalignment condition. By using the proposed design, the equivalent MI M_{eq} is improved to 21.51 μH, where two multiples of M_{fs} are added to M_{ps}. Comparing the gain trends of M_{eq} versus the x- and diagonal misalignments, the maximum variation Δ of M_{eq} is 10.09% from 19.29 to 23.62 μH within $\pm$200-mm misalignment. A change of 4.33 μH is acceptable and within the allowable range in practical applications. In addition, apart from specific misalignment positions, $M_{\mathrm{eq-diag}}$ shows a similar trend with $M_{\mathrm{eq-x}}$ since the diagonal misalignment is composed of equal x- and y-misalignments. Nevertheless, the changes of $M_{\mathrm{eq-y}}$ are not identical in the symmetrical range due to the terminal location of the C-shaped Cx coil, as shown in Fig. 3(a), resulting in a slightly lower $M_{\mathrm{eq-y}}$, as well as a 10.03% variation in $M_{\mathrm{eq-diag}}$. Despite this, $M_{\mathrm{eq-y}}$ indicates a reasonable misalignment tolerance with a maximum $\Delta = 10.18\%$ within a $\pm$180-mm y-misalignment.

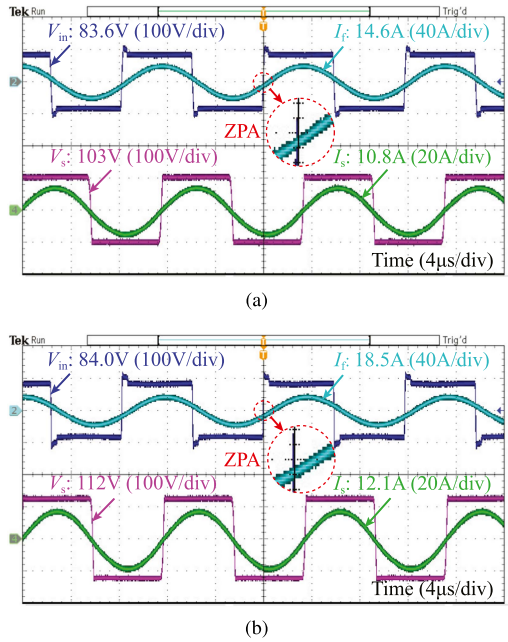

Fig. 8. Steady-state experimental waveforms of $\boldsymbol{V}_{\mathrm{in}}$, $\boldsymbol{I}_{\mathrm{f}}$, $\boldsymbol{V}_{\mathrm{s}}$, and $\boldsymbol{I}_{\mathrm{s}}$ with $R_{\mathrm{B}} = 10\,\Omega$ under (a) 100-mm x-misalignment and (b) 200-mm x-misalignment conditions.

Furthermore, by installing the terminal side of the C-shaped Cx coil perpendicularly to the direction of the vehicle, large y-misalignments can be reasonably avoided. In addition, the overlapped terminal design or changing the connection method between the inner and outer coils of the C-shaped Cx coil can mitigate the effect of the terminal on magnetic coupling, possibly reducing the 15.18% variation of 5.67 μH to accommodate a 200-mm y-misalignment. By ignoring the measurement errors, therefore, the proposed design demonstrates a similar misalignment tolerance under x-, y-, and diagonal misalignments, amounting to approximately 55.6% of the length of the Rx coil.

As analyzed, the horizontal misalignment tolerance of the design is only investigated under x-misalignment. At $R_{\mathrm{B}} = 10\,\Omega$, Fig. 8 provides the steady-state experimental waveforms of the system with 100 and 200-mm x-misalignment. Compared to Fig. 6, the results show that the system can achieve the M_{eq}-independent ZPA input within 55.6% of the length of the Rx coil misalignment range by using the proposed design. Furthermore, the root mean square (RMS) $\boldsymbol{I}_{\mathrm{s}}$ has an acceptable maximum change of 0.7 A from 11.4 to 12.1 A under 200-mm misalignment compared to the perfectly aligned condition. Moreover, the variation in the RMS $\boldsymbol{I}_{\mathrm{s}}$ is amount to 5.68%, spanning from 10.8 to 12.1 A within 200-mm misalignment range. Therefore, the CC output is maintained within 55.6% of the length of the Rx coil misalignment range, verifying the theoretical analysis and the feasibility of the proposed method.

C. Vertical Misalignment Analysis

To evaluate the effectiveness of the proposed misalignment tolerant design, M_{eq} under the vertical misalignment, i.e., z-misalignment, is measured as the air gap changes from 90 to 240 mm with a step size of 10 mm. As provided in Fig. 9, the

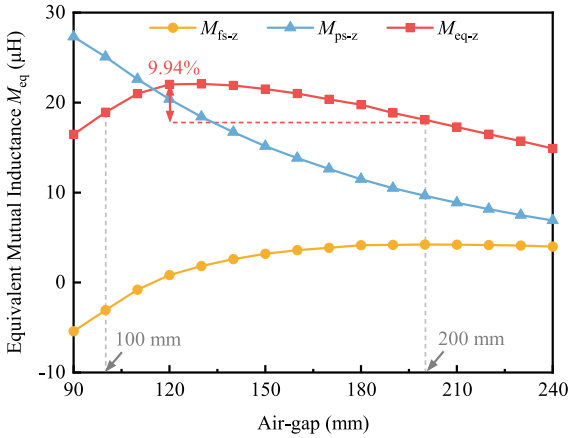

Fig. 9. Variations of M_{eq} versus the z-misalignment.

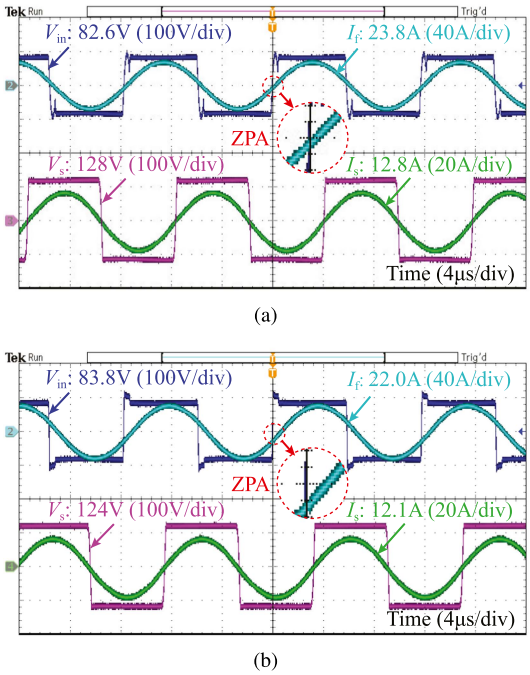

Fig. 10. Steady-state experimental waveforms of $\boldsymbol{V}_{in}$, $\boldsymbol{I}_f$, $\boldsymbol{V}_s$, and $\boldsymbol{I}_s$ with $R_B = 10\,\Omega$ under (a) -50-mm z-misalignment and (b) 50-mm z-misalignment.

opposite gain trends of M_{fs} and M_{ps} versus the misalignment are maintained. Therefore, M_{eq} performs a similar misalignment tolerant profile between the vertical and horizontal misalignments. In other words, under the z-misalignment condition, M_{eq} can be stable by using (22). It can be observed from Fig. 9 that M_{eq} varies from 18.92 μH under 100-mm air gap to 18.08 μH under 200-mm air gap, where the maximum variation is 9.94% of 3.99 μH. Within reasonable limits, the CC output can be maintained within $\pm$50-mm z-misalignment by ignoring the measurement errors.

The experimental verification of the proposed design is carried out under -50 and 50-mm z-misalignment with $R_B = 10\ \Omega$, provided in Fig. 10. As the air gap increases from 100 to 200 mm, the RMS $\boldsymbol{I}_s$ varies from 12.8 to 11.4 A and then to 12.1 A. The maximum change of 1.4 A falls within an acceptable and

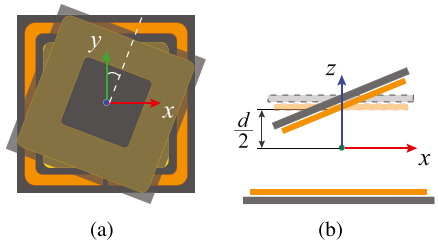

Fig. 11. Angular misalignment rotates around (a) the z-axis and (b) the line: $x = 0, z = d/2$.

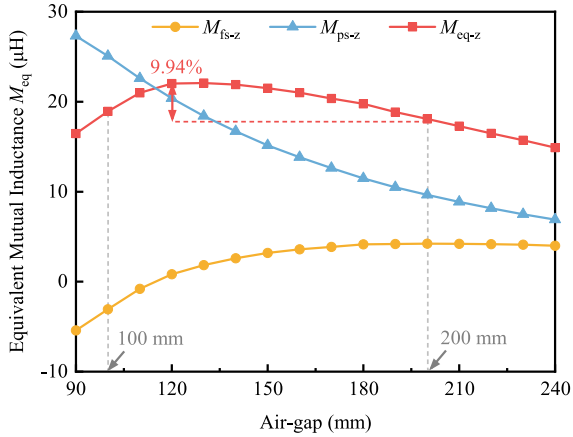

Fig. 12. Variations of M_{eq} versus the angular misalignment.

allowable range in practical applications. This demonstrates that the experimental system can achieve CC output independent of the air gap within $\pm$50-mm z-misalignment. Moreover, under -50-mm z-misalignment, the ZPA input is maintained. As shown in Fig. 10(b), a noticeable phase shift from the perfect ZPA is observed, which is attributed to the change in the resonance state resulting from the alteration of topological parameters under 50-mm z-misalignment. However, the phase shift is minimal, guaranteeing the ZPA input.

D. Angular Misalignment Analysis

Angular misalignment is a common error in the WPT system, which can be modeled as rotation around the z-axis and line: $x = 0, z = d/2$, as depicted in Fig. 11. Given the symmetry of the coil structure, the angular misalignment of M_{eq} is tested within 45° when rotating around the z-axis. However, owing to the mechanical constraint in the experimental setup, measurements are limited to angles up to 20° when rotating around the line: $x = 0, z = d/2$. Based on the results shown in Fig. 12, the maximum changes of M_{eq} are 0.85 and 1.34 μH. These results demonstrate that the proposed complementary coupling design achieved by adding two multiples of M_{fs} to M_{ps} enables the system to maintain a stable M_{eq} in the presence of reasonable angular deviations.

Under the maximum angular misalignment conditions, the ZPA input and CC output characteristics are measured and presented in Fig. 13. It can be observed that the ZPA input can be maintained under both types of angular misalignment. As the

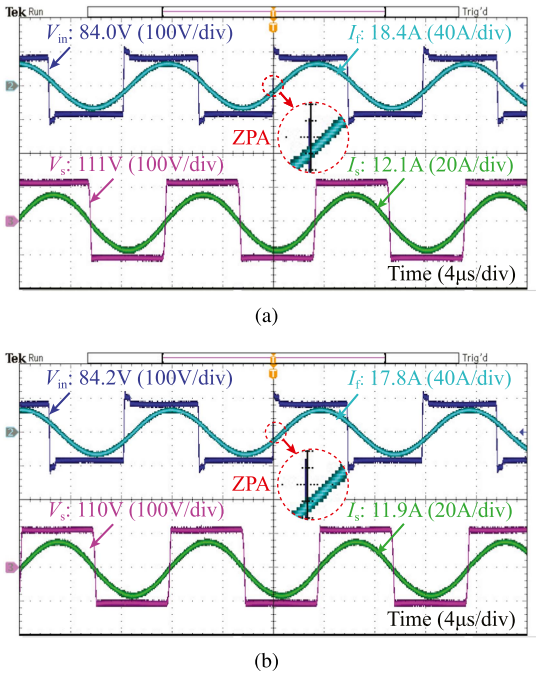

Fig. 13. Steady-state experimental waveforms of $\boldsymbol{V}_{\rm in}$, $\boldsymbol{I}_{\rm f}$, $\boldsymbol{V}_{\rm s}$, and $\boldsymbol{I}_{\rm s}$ with $R_{\rm B} = 10\ \Omega$ under (a) 45° rotation around the z-axis and (b) 20° rotation around the line: $x = 0, z = d/2$.

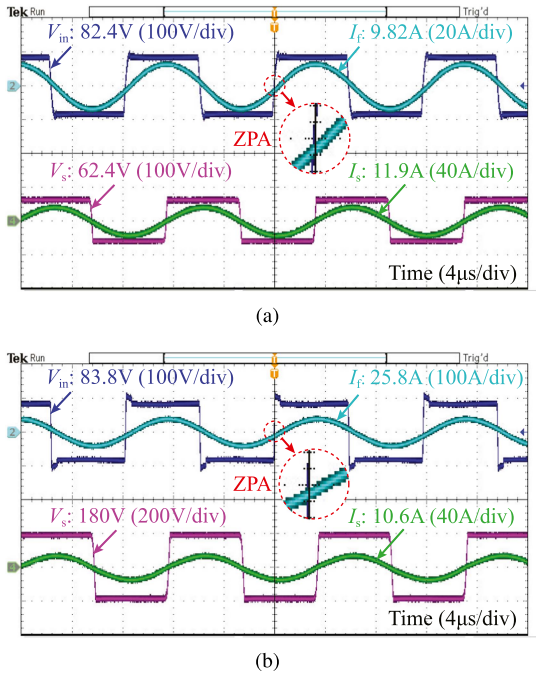

Fig. 14. Steady-state experimental waveforms of $\boldsymbol{V}_{\rm in}$, $\boldsymbol{I}_{\rm f}$, $\boldsymbol{V}_{\rm s}$, and $\boldsymbol{I}_{\rm s}$ with (a) $R_{\rm B} = 5\ \Omega$ and (d) $R_{\rm B} = 20\ \Omega$.

rotation around the z-axis increases to 45°, the RMS $\boldsymbol{I}_{\rm s}$ experiences a change of 6.14% compared with its perfectly aligned position. However, this change is only 0.7 A, which is acceptable in practice. Therefore, the planar rotation misalignment barely affects the system performance. Similarly, the RMS $\boldsymbol{I}_{\rm s}$ has an acceptable change of 4.39% under 20° rotation around the line: $x = 0, z = d/2$. Within reasonable limits, therefore, the system can operate with a CC output within ±20° rotation misalignment around the line: $x = 0, z = d/2$.

E. Performance of the WPT System With Load Variations

The experiments with load variations are conducted and presented in Fig. 14 under the perfectly aligned condition. The results indicate that $\boldsymbol{I}_{\rm f}$ remains in phase with $\boldsymbol{V}_{\rm in}$ throughout the load variations, indicating the achievement of the load-independent ZPA input. By adjusting the electrical dc load, the RMS $\boldsymbol{I}_{\rm s}$ varies from 11.9 A at $R_{\rm B} = 5\ \Omega$ to 10.6 A at $R_{\rm B} = 20\ \Omega$, where the variation $\Delta = 5.78\%$. In comparison to the nominal condition, these changes correspond to 4.39% and 7.02% variations, respectively. These findings highlight that the system, built based on the proposed design strategy, is capable of delivering a load-independent CC output with ZPA input conditions.

F. Output Power and System Efficiency

The output power and efficiency of the proposed system under different misalignments at $R_{\rm B} = 10\ \Omega$ are provided in Fig. 15, where the trends of η and $P_{\rm o}$ can be explained by

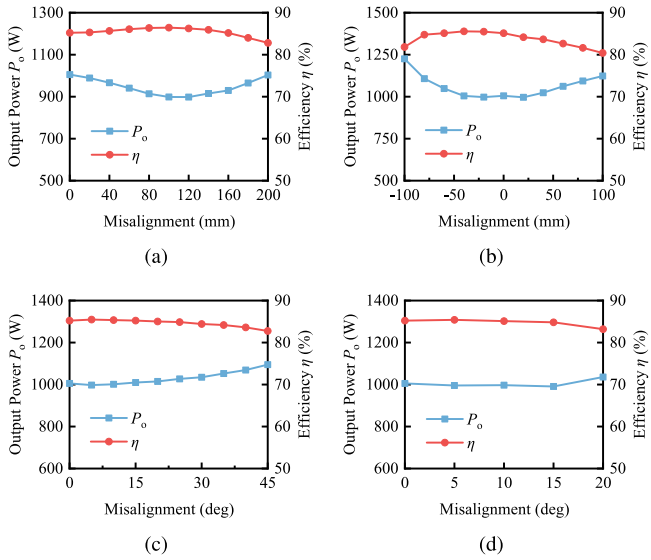

Fig. 15. Output power and DC–DC efficiency versus (a) x-misalignment, (b) z-misalignment, (c) rotation around the z-axis, and (d) rotation around the line: $x = 0, z = d/2$.

the changes of $M_{\rm eq}$ versus the misalignment. It can be observed that the system efficiency stays approximately constant, even with a maximum change of 5.15% under the z-misalignment. Furthermore, the dc–dc efficiency η has a maximum value of 86.44% under 100-mm x-misalignment. Meanwhile, it can be maintained at over 80% within the misalignment tolerance range, which complies with the SAE J2954 and acceptable for a noncontrol WPT system. Under the perfectly aligned position, the output power $P_{\rm o}$ is 1005.28 W with $\eta = 85.22\%$, which has a maximum variation

TABLE III
COMPARISON WITH OTHER METHODS

Items	Coil size and air gap (mm)	Distance-to-diameter ratio	Output power (W)	Efficiency	ZPA	Output type	Misalignment tolerant range (mm)	Angular misalignment tolerance (non-planar rotation)	Decoupling	Complementary and increased MI
[19]	Primary: 400 (diameter) Secondary: 300 (diameter) Air gap: 100	0.333	800	90.11%	No	CV	x-misalignment: $\pm$100 (33%) y-misalignment: $\pm$100 (33%) z-misalignment: $-40 \sim +50$	No	No	No
[20]	Primary: 512 × 248 Secondary: 326 × 248 Air gap: 150	0.460	600	91%	Yes	CV	x-misalignment: $\pm$180 (35.2%) y-misalignment: $\pm$75 (30.2%) z-misalignment: N/A	No	Yes	Yes
[21]	Primary: 775 × 391 Secondary: 775 × 391 Air gap: 120	0.155	3300	94%	No	CP (constant power)	x-misalignment: $-80 \sim +120$ y-misalignment: $\pm$160 (50%) z-misalignment: $\pm$20	No	No	No
[22]	Primary: 450 × 450 Secondary: 400 × 400 Air gap: 150	0.375	3443	92.1%	Yes	CC	x-misalignment: $\pm$180 (40%) y-misalignment: $\pm$180 (40%) z-misalignment: N/A	No	No	No
[23]	Primary: 450 × 450 Secondary: 400 × 400 Air gap: 150	0.375	1003.27	91.17%	Yes	CC	x-misalignment: $\pm$200 (50%) y-misalignment: $\pm$200 (50%) z-misalignment: N/A	No	No	No
[24]	Primary: 280 × 280 Secondary: 280 × 280 Air gap: 100	0.375	201.9	81.12%	Yes	CC	x-misalignment: $\pm$140 (50%) y-misalignment: $\pm$140 (50%) z-misalignment: $-20 \sim +15$	No	Yes	No
[28]	Primary: 400 × 400 Secondary: 400 × 400 Air gap: 150	0.375	3500	96.31%	Yes	CC	x-misalignment: $\pm$200 (50%) y-misalignment: $\pm$45 (11.3%) z-misalignment: $-45 \sim +30$	No	No	Yes
[29]	Primary: 400 × 400 Secondary: 400 × 400 Air gap: 150	0.375	3500	93.96%	Yes	CV	x-misalignment: $\pm$150 (37.5%) y-misalignment: $\pm$150 (37.5%) z-misalignment: $-20 \sim +35$	No	Yes	No
[31]	Primary: 400 × 400 Secondary: 400 × 400 Air gap: 200	0.5	700	93.14%	No	CV	x-misalignment: $\pm$200 (50%) y-misalignment: $\pm$150 (37.5%) z-misalignment: N/A	No	Yes	Yes
This work	**Primary: 460 × 460 Secondary: 360 × 360 Air gap: 150**	**0.417**	**1005.28**	**85.22%**	**Yes**	**CC**	**x-misalignment: $\pm$180 (55.6%) y-misalignment: $\pm$180 (55.6%) z-misalignment: $\pm$50**	**Yes**	**No**	**Yes**

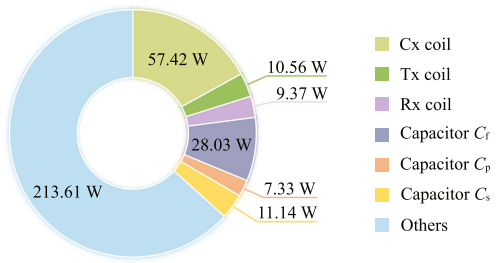

Fig. 16. Power losses of the proposed system under rated condition.

of $\Delta = 10.32\%$ under the z-misalignment. Considering the measurement errors, the output power P_o can be maintained stable under the misalignment conditions within reasonable limits.

The power losses in the topology, as shown in Fig. 16, are much lower compared to the 213.61-W loss caused by components, such as magnetic cores and semiconductors. Meanwhile, the ac–ac efficiency can reach over 92% under the rated condition, as shown in Fig. 6. As demonstrated by the proof-of-concept prototype, the proposed strategy has been proven to be effective and practical. Future works on optimizing the shielding structure, equipment, and controller can be investigated to improve system efficiency, reduce losses, and enhance system performance.

G. Comparison With Other Methods

A comprehensive performance comparison between the proposed and other misalignment tolerant design methods is given in Table III, in which the percentages of the x- and y-misalignment tolerance are relative to the Rx coil dimension. Define the distance-to-diameter ratio as the ratio of the air gap to the maximum length of the Rx coil. Upon reviewing the table, it is evident that the proposed design offers superior tolerance to z- and angular misalignments compared to previous methods in [19], [21], [22], and [23]. While methods in [19], [21], and [22] achieve higher efficiency, their performance is limited to a smaller distance-to-diameter ratio. In addition, these methods do not achieve the ZPA input condition or consider load independence. In comparison to methods in [23], [24], and [29], the proposed design exhibits higher tolerance to x- and y-misalignments with a large distance-to-diameter ratio and comparable efficiency. Moreover, the proposed design avoids the reduction in the MI caused by the reverse-series structure, which is observed in [23] and [24]. Meanwhile, compared to [29], the proposed design does not incorporate any coil decoupling. In [28], the DD pad can provide the complementary MI. Nevertheless, it only works when there is a y-misalignment to maintain the MI to the same level as the perfectly aligned condition, which cannot be used to increase the equivalent MI. Similarly, the coupling complement effect works only when there is an x-misalignment in [20], where the decoupling design should be considered. Although the method in [31] achieves a higher efficiency with a larger distance-to-diameter ratio, the proposed design outperforms the method in [31] in terms of x- and y-misalignment tolerance, particularly in the y-misalignment. Furthermore, the tolerance in z- and angular misalignments is not considered, and the two Rxs cannot tolerate the x-misalignment simultaneously [31]. The distinguished contribution of this article lies in the development of a complementary coupling

integration strategy that enhances both misalignment tolerance and power delivery capacity.

V. Conclusion

This article introduces a complementary coupling integration strategy for LCC-S-compensated WPT systems, aiming to improve misalignment performance and system transfer capacity. This article provides a detailed analysis of the new integrated coil topology and its Cx method, which incorporates ZPA input and load-independent CC output.

The proposed design features a Cx coil constructed using a long rectangular coil wound on a C-shaped structure. This design enables the achievement of complementary MIs between the Tx and Rx coils, as well as between the Cx and Rx coils. These MIs exhibit opposite gain trends relative to misalignment, and their combined effects are multiplied, thereby enhancing the equivalent MI of the system. This approach outperforms hybrid topologies, improving the equivalent MI in both the perfectly aligned and misaligned conditions.

Furthermore, the proposed design offers a higher transfer capacity compared to previous methods due to the increased equivalent MI achieved through the complementary coupling effect. To validate the theoretical analyses, a scaled-down prototype with a power rating of 1 kW is built based on the proposed design. The experimental results demonstrate the feasibility and practicality of the approach, highlighting its potential for high-power WPT systems that require stable output performance even under significant misalignment conditions.

A limitation of the proposed method is its sensitivity to y-misalignment, primarily caused by the terminal of the Cx coil. However, there are potential avenues for improving the system performance through optimization. One approach is to modify the Cx coil's terminal, such as by redesigning it to overlap or changing the connection method between its inner and outer coils. By exploring these additional optimization techniques, it is possible to enhance the system performance to better suit specific applications. Further research and development on this front hold the potential for achieving significant improvements in the future.

References

[1] H. Feng, R. Tavakoli, O. C. Onar, and Z. Pantic, "Advances in high-power wireless charging systems: Overview and design considerations," *IEEE Trans. Transp. Electrific.*, vol. 6, no. 3, pp. 886–919, Sep. 2020.

[2] V. B. Vu et al., "Operation of inductive charging systems under misalignment conditions: A review for electric vehicles," *IEEE Trans. Transp. Electrific.*, vol. 9, no. 1, pp. 1857–1887, Mar. 2023.

[3] X. Wang, J. Xu, M. Leng, H. Ma, and S. He, "A hybrid control strategy of LCC-S compensated WPT system for wide output voltage and ZVS range with minimized reactive current," *IEEE Trans. Ind. Electron.*, vol. 68, no. 9, pp. 7908–7920, Sep. 2021.

[4] W. Li, Q. Zhang, C. Cui, and G. Wei, "A self-tuning S/S compensation WPT system without parameter recognition," *IEEE Trans. Ind. Electron.*, vol. 69, no. 7, pp. 6741–6750, Jul. 2022.

[5] Z. Luo, Y. Zhao, M. Xiong, X. Wei, and H. Dai, "A self-tuning LCC/LCC system based on switch-controlled capacitors for constant-power wireless electric vehicle charging," *IEEE Trans. Ind. Electron.*, vol. 70, no. 1, pp. 709–720, Jan. 2023.

[6] C. Xiao, B. Cao, and C. Liao, "A fast construction method of resonance compensation network for electric vehicle wireless charging system," *IEEE Trans. Instrum. Meas.*, vol. 70, 2021, Art no. 2003309.

[7] Z. Zhang, F. Zhu, D. Xu, P. T. Krein, and H. Ma, "An integrated inductive power transfer system design with a variable inductor for misalignment tolerance and battery charging applications," *IEEE Trans. Power Electron.*, vol. 35, no. 11, pp. 11544–11556, Nov. 2020.

[8] S. Luo, Z. Yao, Z. Zhang, G. Li, X. Zhang, and H. Ma, "A dual shunt inductor compensated IPT system with nearly unity power factor for wide load range and misalignment tolerance," *IEEE Trans. Ind. Electron.*, vol. 69, no. 10, pp. 10001–10013, Oct. 2022.

[9] H. Feng, T. Cai, S. Duan, X. Zhang, H. Hu, and J. Niu, "A dual-side-detuned series–series compensated resonant converter for wide charging region in a wireless power transfer system," *IEEE Trans. Ind. Electron.*, vol. 65, no. 3, pp. 2177–2188, Mar. 2018.

[10] Y. Wang, J. Mai, Y. Yao, and D. Xu, "Analysis and design of an IPT system based on S/SP compensation with improved output voltage regulation," *IEEE Trans. Ind. Informat.*, vol. 16, no. 5, pp. 3256–3266, May 2020.

[11] Y. Yao, Y. Wang, X. Liu, Y. Pei, D. Xu, and X. Liu, "Particle swarm optimization-based parameter design method for S/CLC-compensated IPT systems featuring high tolerance to misalignment and load variation," *IEEE Trans. Power Electron.*, vol. 34, no. 6, pp. 5268–5282, Jun. 2019.

[12] A. Ramezani, S. Farhangi, H. Iman-Eini, B. Farhangi, R. Rahimi, and G. R. Moradi, "Optimized-LCC-series compensated resonant network for stationary wireless EV chargers," *IEEE Trans. Ind. Electron.*, vol. 66, no. 4, pp. 2756–2765, Apr. 2019.

[13] F. Wang, W. Zhang, L. Ye, J. Guo, K. Liu, and H. T. Do, "A design method to implement ZVS for electric vehicle wireless charging system with double-side LCC compensation," *IEEE Trans. Emerg. Sel. Topics Power Electron.*, vol. 9, no. 3, pp. 3791–3801, Mar. 2021.

[14] J. Mai, Y. Wang, Y. Yao, and D. Xu, "Analysis and design of high-misalignment-tolerant compensation topologies with constant-current or constant-voltage output for IPT systems," *IEEE Trans. Power Electron.*, vol. 36, no. 3, pp. 2685–2695, Mar. 2021.

[15] H. Feng, A. Dayerizadeh, and S. M. Lukic, "A coupling-insensitive X-type IPT system for high position tolerance," *IEEE Trans. Ind. Electron.*, vol. 68, no. 8, pp. 6917–6926, Aug. 2021.

[16] Y. Chen et al., "Reconfigurable topology for IPT system maintaining stable transmission power over large coupling variation," *IEEE Trans. Power Electron.*, vol. 35, no. 5, pp. 4915–4924, May 2020.

[17] Y. Zhang et al., "Misalignment-tolerant dual-transmitter electric vehicle wireless charging system with reconfigurable topologies," *IEEE Trans. Power Electron.*, vol. 37, no. 8, pp. 8816–8819, Aug. 2022.

[18] M. Wu et al., "A compact coupler with integrated multiple decoupled coils for wireless power transfer system and its anti-misalignment control," *IEEE Trans. Power Electron.*, vol. 37, no. 10, pp. 12814–12827, Oct. 2022.

[19] S. J. Huang, T. S. Lee, Y. M. Yang, and J. Y. Chen, "Intermediate coil-aided wireless charging via interactive power transmitting with misalignment-tolerating considerations," *IEEE Trans. Ind. Electron.*, vol. 69, no. 10, pp. 9972–9983, Oct. 2022.

[20] N. Rasekh, J. Kavianpour, and M. Mirsalim, "A novel integration method for a bipolar receiver pad using LCC compensation topology for wireless power transfer," *IEEE Trans. Veh. Technol.*, vol. 67, no. 8, pp. 7419–7428, Aug. 2018.

[21] L. Zhao, D. J. Thrimawithana, U. K. Madawala, A. P. Hu, and C. C. Mi, "A misalignment-tolerant series-hybrid wireless EV charging system with integrated magnetics," *IEEE Trans. Power Electron.*, vol. 34, no. 2, pp. 1276–1285, Feb. 2019.

[22] Y. Chen, R. Mai, Y. Zhang, M. Li, and Z. He, "Improving misalignment tolerance for IPT system using a third-coil," *IEEE Trans. Power Electron.*, vol. 34, no. 4, pp. 3009–3013, Apr. 2019.

[23] P. Zhang, M. Saeedifard, O. C. Onar, Q. Yang, and C. Cai, "A field enhancement integration design featuring misalignment tolerance for wireless EV charging using LCL topology," *IEEE Trans. Power Electron.*, vol. 36, no. 4, pp. 3852–3867, Apr. 2021.

[24] Z. Yuan, M. Saeedifard, C. Cai, Q. Yang, P. Zhang, and H. Lin, "A misalignment tolerant design for a dual-coupled LCC-S-compensated WPT system with load-independent CC output," *IEEE Trans. Power Electron.*, vol. 37, no. 6, pp. 7480–7492, Jun. 2022.

[25] G. Li and H. Ma, "A hybrid IPT system with high-misalignment tolerance and inherent CC–CV output characteristics for EVS charging applications," *IEEE Trans. Emerg. Sel. Topics Power Electron.*, vol. 10, no. 3, pp. 3152–3160, Mar. 2022.

[26] Y. Wang, H. Liu, H. Yu, P. Wheeler, Q. Zhou, and S. Zhao, "A hybrid battery wireless charger for self-adapting battery charging curve and anti-misalignment," *IEEE J. Emerg. Sel. Topics Ind. Electron.*, early access, doi: 10.1109/JESTIE.2023.3270843.
[27] L. Ji, M. Zhang, B. Qian, and H. Sun, "A series of hybrid WPT systems with automatic switching between constant-current and constant-voltage modes on the secondary side," *IEEE Trans. Emerg. Sel. Topics Power Electron.*, vol. 11, no. 1, pp. 361–371, Jan. 2023.
[28] B. Yang, Y. Chen, W. Ruan, H. Liu, Y. Ren, and R. Mai, "Current stress optimization for double-sided CLLLC topology-based IPT system with constant output current tolerating pad misalignments," *IEEE Trans. Ind. Appl.*, vol. 58, no. 1, pp. 1032–1043, Jan./Feb. 2022.
[29] Y. Chen et al., "A hybrid inductive power transfer system with misalignment tolerance using quadruple-D quadrature pads," *IEEE Trans. Power Electron.*, vol. 35, no. 6, pp. 6039–6049, Jun. 2020.
[30] X. Qu, Y. Yao, D. Wang, S. C. Wong, and C. K. Tse, "A family of hybrid IPT topologies with near load-independent output and high tolerance to pad misalignment," *IEEE Trans. Power Electron.*, vol. 35, no. 7, pp. 6867–6877, Jul. 2020.
[31] A. Hossain, P. Darvish, S. Mekhilef, K. S. Tey, and C. W. Tong, "A new coil structure of dual transmitters and dual receivers with integrated decoupling coils for increasing power transfer and misalignment tolerance of wireless EV charging system," *IEEE Trans. Ind. Electron.*, vol. 69, no. 8, pp. 7869–7878, Aug. 2022.
[32] W. Shi et al., "Design of a highly efficient 20-kW inductive power transfer system with improved misalignment performance," *IEEE Trans. Transp. Electrific.*, vol. 8, no. 2, pp. 2384–2399, Feb. 2022.

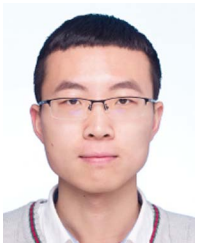

Zhaoyang Yuan (Member, IEEE) received the B.S. degree in electrical engineering and the M.S. degree in control science and engineering from Tiangong University, Tianjin, China, in 2015 and 2018, respectively. He is currently working toward the Ph.D. degree in electrical engineering with the Hebei University of Technology, Tianjin.

From 2019 to 2021, he was a Visiting Researcher with the School of Electrical and Computer Engineering, Georgia Institute of Technology, Atlanta, GA, USA. His research interests include engineering electromagnetism, power electronics, wireless power transfer, and its industrial applications.

Qingxin Yang received the B.S., M.S., and Ph.D. degrees in electrical engineering from the Hebei University of Technology, Tianjin, China, in 1983, 1986, and 1997, respectively.

Since 1996, he has been a Professor with the Hebei University of Technology. From 2008 to 2018, he was the President with Tianjin Polytechnic University, Tianjin. He is currently with the Tianjin University of Technology, Tianjin, where he was the President from 2018 to 2020. His research interests include computational electromagnetism, wireless power transfer, and engineering electromagnetism applications.

Dr. Yang was a Board Member of the International Compumag Society and the President of the China chapter. Since 2015, he has been the President of the China Electrotechnical Society.

Xian Zhang received the M.E. and Ph.D. degrees in electrical engineering from the Hebei University of Technology, Tianjin, China, in 2009, and 2012, respectively.

He is currently a Professor with the Hebei University of Technology. He is the Director of the China Electrotechnical Society and the Secretary-General of the National Specialized Committee on Wireless Power Transmission Technology. His research interests encompass intelligent high-power wireless power transmission technology, measurement of 3-D electromagnetic fields, and numerical calculations of modern engineering electromagnetic fields.

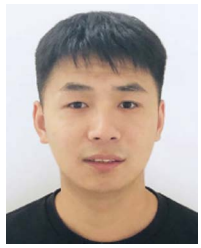

Ran Wang received the B.S. degree in electrical engineering from Shandong Jianzhu University, Jinan, China, in 2021. He is currently working toward the M.E. degree in electrical engineering with the Hebei University of Technology, Tianjin, China.

His research interests include engineering electromagnetism, wireless power transfer, and its industrial applications.

Xianjie Ma received the B.S. degree in electronic engineering from the Qingdao University of Science and Technology, Qingdao, China, in 2021. He is currently working toward the M.E. degree in electrical engineering with the Hebei University of Technology, Tianjin, China.

His research interests include engineering electromagnetism, wireless power transfer, and its industrial applications.

Changsong Cai (Senior Member, IEEE) received the Ph.D. degree in electrical engineering from Wuhan University, Wuhan, China, in 2020.

He is currently a Postdoctoral Research Fellow with the School of Electrical Engineering and Automation, Wuhan University. From 2019 to 2020, he was a Visiting Researcher with the School of Electrical and Computer Engineering, Georgia Institute of Technology, Atlanta, GA, USA. His research interests include engineering electromagnetism, power electronics, wireless power transfer, and its industrial applications.

Dr. Cai was the recipient of the First Place Prize Paper Award from IEEE TRANSACTIONS ON POWER ELECTRONICS in 2022.

Pengcheng Zhang (Senior Member, IEEE) received the B.S. degree in electrical engineering and the M.S. degree in control science and engineering from Tiangong University, Tianjin, China, in 2013 and 2016, respectively, and the Ph.D. degree in electrical engineering from the Hebei University of Technology, Tianjin, China, in 2021.

From 2017 to 2019, he was a Visiting Researcher with the School of Electrical and Computer Engineering, Georgia Institute of Technology, Atlanta, GA, USA. He is currently a Postdoctoral Researcher with the Department of Electrical Engineering, Tsinghua University, Beijing, China. His research interests include wireless power transfer and electromagnetic shielding.

Dr. Zhang was the recipient of the First Place Prize Paper Award from IEEE TRANSACTIONS ON POWER ELECTRONICS in 2022.

Hongjian Lin (Senior Member, IEEE) received the Ph.D. degree in electrical engineering from Southwest Jiaotong University, Chengdu, China, in 2021.

From 2019 to 2020, he was a Visiting Researcher with the School of Electrical and Computer Engineering, Georgia Institute of Technology, Atlanta, GA, USA. From 2021 to 2022, he was a Postdoctoral Research Associate with the Department of Electrical Engineering, Hong Kong Polytechnic University, Hong Kong. He is currently a Postdoctoral Research Fellow with the Department of Electrical Engineering, City University of Hong Kong, Hong Kong. His research interests include model-predictive control of converters in microgrids, electrical machines and drives control, electric traction supply systems, and modulation and control technologies of multilevel converters in the solid-state transformer.

Maryam Saeedifard (Fellow, IEEE) received the Ph.D. degree in electrical engineering from the University of Toronto, Toronto, ON, Canada, in 2008.

Since 2014, she has been with the School of Electrical and Computer Engineering, Georgia Institute of Technology, Atlanta, GA, USA, where she is currently a Professor and holds a Dean's professorship. Her research interests include power electronics and its applications in terrestrial and mobile power systems.

Dr. Saeedifard is the recipient of the Roger Webb's Excellence in Mentorship Award from the School of Electrical and Computer Engineering, Georgia Tech in 2023, the 8th Nagamori Award from Nagamori Foundation in 2022, the Roger Webb's Outstanding Mid-Career Faculty Award from the School of Electrical and Computer Engineering, Georgia Tech in 2021, the U.S. Clean Energy Education and Empowerment Technology Research and Innovation Award from the Department of Energy in 2021, the First Place Prize Paper Award from IEEE TRANSACTIONS ON POWER ELECTRONICS in 2023, 2022, and 2021, the Best Transactions Paper Award of IEEE TRANSACTIONS ON INDUSTRIAL ELECTRONICS in 2018 and 2016, the IEEE J. David Irwin Early Career Award in 2018, the U.S. National Academy of Engineering Frontiers in Engineering in Education in 2012, the U.S. National Academy of Engineering Frontiers in Engineering in 2011, the Excellence in Research Award from the Office of Vice-President in Research at Purdue University in 2011 and 2012, and the IEEE Richard M. Bass Outstanding Young Power Electronic Engineer Award in 2010. She is a Co-Editor-in-Chief for IEEE TRANSACTIONS ON POWER ELECTRONICS.